

# Spectral mixture analysis of ASTER images for examining the relationship between urban thermal features and biophysical descriptors in Indianapolis, Indiana, USA

Dengsheng Lu<sup>a,\*</sup>, Qihao Weng<sup>b</sup>

<sup>a</sup> Center for the Study of Institutions, Population, and Environmental Change (CIPEC), Indiana University, Bloomington, IN 47408, USA

<sup>b</sup> Department of Geography, Geology, and Anthropology, Indiana State University, Terre Haute, IN 47809, USA

Received 10 February 2005; received in revised form 8 November 2005; accepted 22 November 2005

## Abstract

Mapping urban biophysical and thermal conditions has attracted increasing interest. However, the relationship between them has not been fully understood. This paper explores thermal features and their relationship with biophysical descriptors in an urban environment by analyzing multitemporal ASTER images. Linear spectral mixture analysis was used to unmix the five thermal infrared bands of ASTER into hot-object and cold-object fraction images and to unmix the nine visible, near-infrared, and shortwave-infrared bands into impervious surface, green vegetation, and soil fractions. Land surface temperatures (LSTs) were computed from band 13 (10.25–10.95  $\mu\text{m}$ ) of the ASTER. Correlation analysis was then conducted to examine the relationship between LST and the five derived fraction variables across the spatial resolution of the pixels from the ASTER images, which ranged from 15 m to 90 m. Multiple regression models were further developed to reveal how LSTs were related to urban biophysical descriptors (i.e., impervious surface, green vegetation, and soil) and to the thermal feature fractions (i.e., hot-object and cold-object). Results indicate that impervious surface was positively correlated while vegetation was negatively correlated with LST. Hot objects displayed a more significant role in influencing LST patterns than cold objects.

© 2006 Elsevier Inc. All rights reserved.

**Keywords:** ASTER imagery; Spectral mixture analysis; Land surface temperature; Urban biophysical descriptors; Urban thermal features

## 1. Introduction

Urban heat island (UHI) effect is closely related to many important issues, such as urban climatology, environmental change, and human–environment interactions, affecting the quality of human life. UHI research has attracted increasing interest (Douset & Gourmelon, 2003; Gallo & Owen, 2002; Weng, 2003; Weng et al., 2004). Different approaches, such as field measurement, remote sensing-based approaches, and modeling, have been used to analyze UHI characteristics (Klysik & Fortuniak, 1999; Lo et al., 1997; Quattrochi & Goel, 1995; Quattrochi & Luvall, 1999; Streutker, 2003; Voogt

& Oke, 2003). Remotely sensed thermal infrared (TIR) images have been extensively used for UHI studies. For example, data from the National Oceanic and Atmospheric Administration/Advanced Very High Resolution Radiometer (NOAA AVHRR) are frequently used at the national or global scale (Gallo et al., 1993; Gallo & Owen, 2002; Roth et al., 1989; Streutker, 2003), while Landsat Thematic Mapper (TM) TIR imagery is used at the regional or local scale (Carnahan & Larson, 1990; Kim, 1992; Larson & Carnahan, 1997; Weng, 2001, 2003). As data from the Moderate Resolution Imaging Spectroradiometer (MODIS) and Advanced Spaceborne Thermal Emission and Reflection Radiometer (ASTER) have become readily available in recent years, multiple TIR bands in these sensors may provide better results for UHI studies at various spatial scales. The extraction of land surface temperatures (LST) from remotely sensed TIR data and the extraction of biophysical descriptors from visible near-infrared (VNIR) and shortwave-infrared

\* Corresponding author. Current affiliation: Anthropological Center for Training and Research on Global Environmental Change (ACT), Indiana University, Bloomington, IN 47405, USA.

E-mail address: [dlu@indiana.edu](mailto:dlu@indiana.edu) (D. Lu).

(SWIR) images have been explored separately in previous research, but the relationship between LST and biophysical descriptors has not been completely understood. A better understanding of the interactions between LST and urban biophysical descriptors is essential in advancing UHI studies and those studies related to climatic change and urban ecosystems.

Linear spectral mixture analysis (LSMA) is a physically based image processing technique, which supports repeatable and accurate extraction of quantitative subpixel information (Smith et al., 1990). The LSMA approach has been used for urban studies to extract biophysical descriptors, such as vegetation cover, impervious surface, and soil (Lu & Weng, 2004; Phinn et al., 2002; Rashed et al., 2001, 2003; Small, 2001, 2002; Wu, 2004; Wu & Murray, 2003). The relationship between LST and vegetation cover has been frequently studied by using vegetation indices such as the Normalized Difference Vegetation Index (NDVI). A recent study indicates that NDVI does not provide areal estimates of the amount of vegetation (Small, 2001). More quantitatively and physically based measures of vegetation abundance are needed for applications that require biophysical measures (Small, 2001). Weng et al. (2004) found that LST possesses a slightly stronger negative correlation with vegetation fraction derived from a spectral mixture model than with NDVI for all land-cover types across the image pixel sizes from 30 m to 960 m.

The majority of previous research using LSMA is based on VNIR and SWIR bands, because current remote sensors mainly gather information in multispectral visible, near infrared (NIR), and SWIR bands, with none or one TIR band. Rarely has research relevant to LSMA used TIR images (Collins et al., 2001; Gillespie, 1992). Since ASTER imagery contains nine VNIR and SWIR bands and five TIR bands, both

urban biophysical descriptors and thermal features can be extracted from them. These image transformations would allow the relationship between LST and biophysical descriptors to be examined. Although MODIS data have multiple bands in VNIR, SWIR, and TIR wavelengths, their coarse spatial resolutions (i.e., 250 m for bands 1 and 2, 500 m for bands 3–7, and 1000 m for bands 8–36) may be more suitable for continental- or global-scale studies related to Earth surface and thermal features than for local and regional scales. The ASTER data, with spatial resolutions from 15 m to 90 m, can provide much more detailed information than MODIS, and thus ASTER data are more suitable for the urban-related studies at local and regional scales. Hence, for this paper we used ASTER data to explore the urban thermal features through the analysis of LST and thermal fraction images, and to explore the relationships between urban thermal features and biophysical descriptors. The ASTER TIR bands were used to compute LST and to extract thermal fraction images, and the ASTER VNIR and SWIR bands were used to develop vegetation, impervious surface, and soil fraction images. Correlation and regression analyses were further conducted to explore the relationship between LST, biophysical descriptors, and thermal fractions in an urban environment in the city of Indianapolis, Indiana, USA.

## 2. Study area and data sets

### 2.1. Study area

The city of Indianapolis in Marion County, Indiana, USA was chosen as the study area (Fig. 1). Indianapolis, the state capital, is a key center for manufacturing, warehousing,

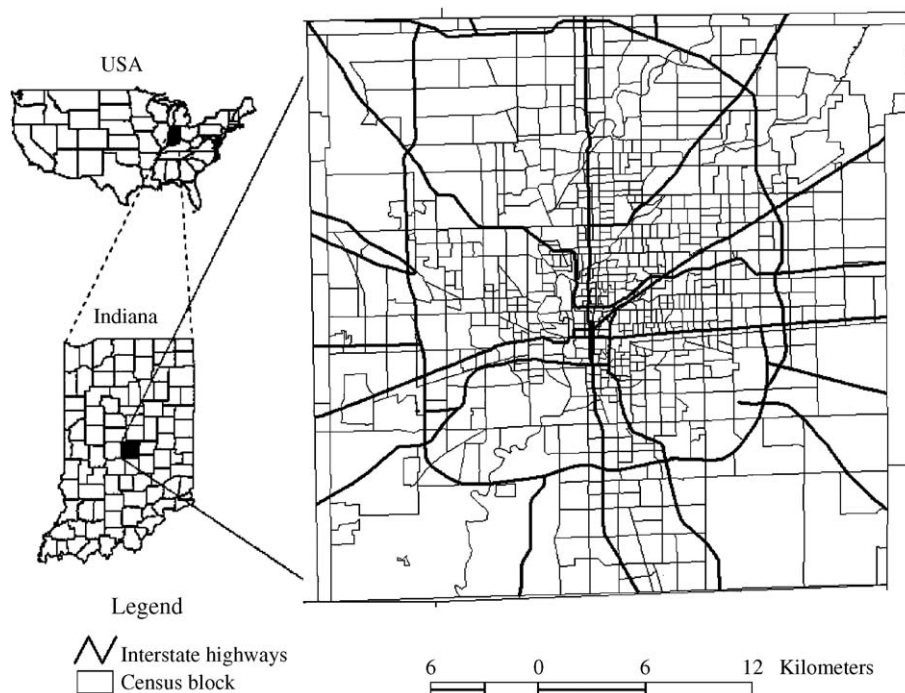


Fig. 1. Map of the study area.

distribution, and transportation in the state. With a population of almost 800,000, it is the twelfth largest city in the USA. It possesses several other advantages that make it an appropriate choice for such a study. It has a single urban core, and other large urban areas in the vicinity have not influenced its growth. The city is located in a flat plain and is relatively symmetrical, having possibilities of expansion in all directions. Like most American cities, Indianapolis is increasing in population and in area. The areal expansion is through encroachment into the adjacent agricultural and rural regions. Certain decision-making forces such as density of population, distance to work, property value, and income structure encourage some sectors of metropolitan Indianapolis to expand faster than others. Detecting and analyzing its urban thermal landscape is significant to control and plan the city's future development.

## 2.2. Data set

Two ASTER images, which were acquired on October 3, 2000, and June 25, 2001, were used in this research. ASTER data have 14 bands with different spatial resolutions, i.e., two visible bands and one NIR band with 15-m spatial resolution,

six SWIR bands with 30-m spatial resolution, and five TIR bands with 90-m spatial resolution (Abrams, 2000; Yamaguchi et al., 1998). We purchased the level 1B (L1B) ASTER data, which consisted of the image data, radiance conversion coefficients, and ancillary data (Fujisada, 1998). When the ASTER image with its HDF file format was imported into IMAGINE reference, an automatic conversion was conducted, which converted the ASTER digital numbers (DNs) to radiance. The separate single bands of VNIR, SWIR, and TIR data were first stacked into one file so that all bands had a pixel size of 15 m by 15 m to preserve the spatial features provided in the VNIR bands. Although the geometric correction was done with the L1B ASTER data product, the position accuracy was not sufficiently high because ground control points were not used during the preprocessing stage. Visually checking the ASTER images and corresponding ETM+ images, which already had been geometrically rectified using control points collected from 1:24,000 scale topographic maps, indicated that position errors of 2–3 pixels existed in the two ASTER images. An image-to-image registration was conducted between the ASTER images and the ETM+ image in order to keep registration errors to less than half a pixel. During the image registration, the nearest-

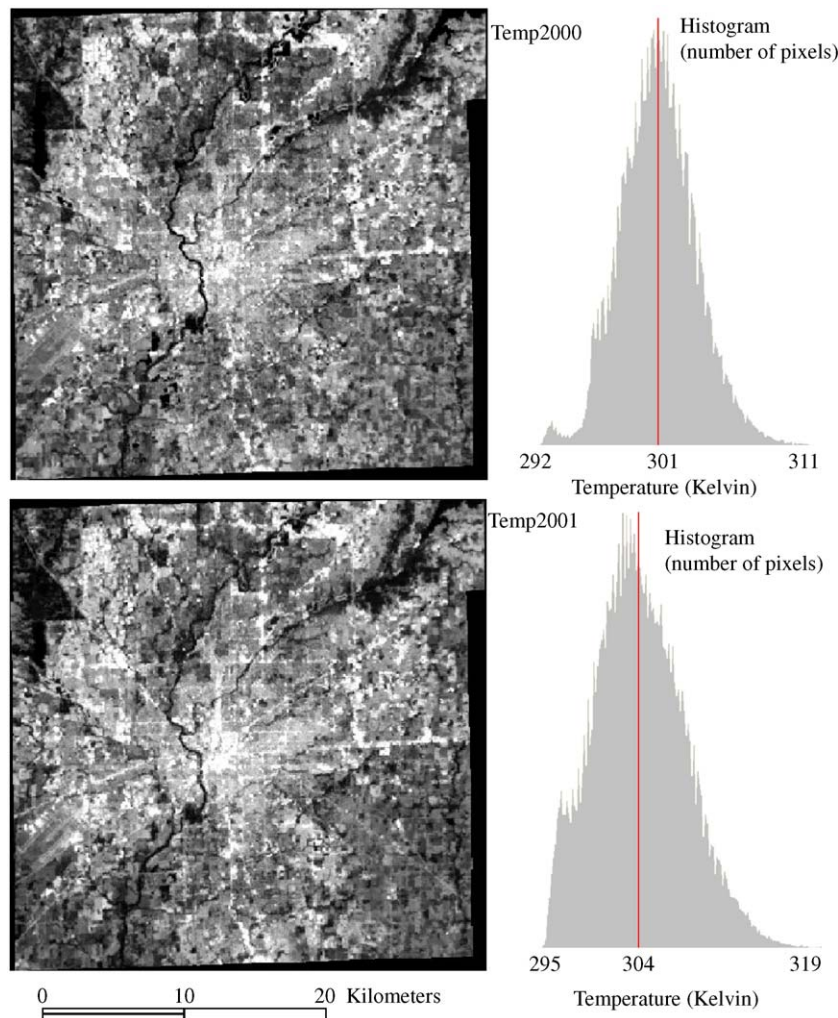


Fig. 2. Land surface temperature distributions and associated histograms in October 3, 2000, and June 25, 2001.

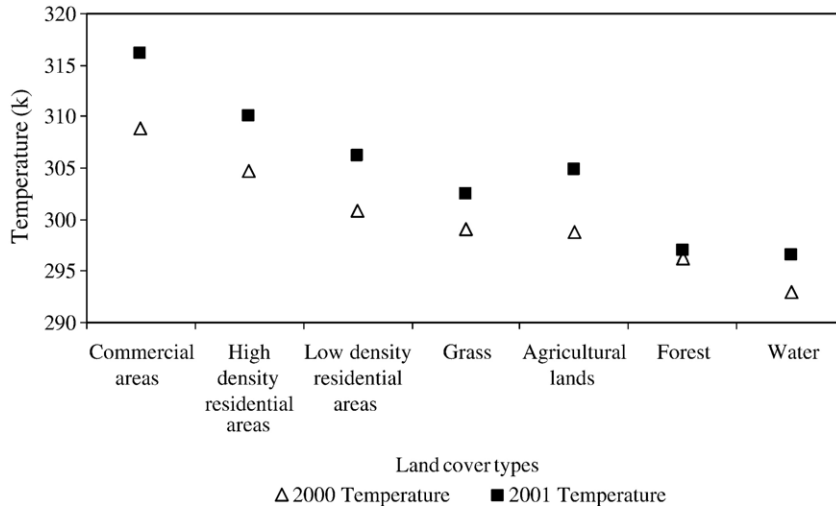


Fig. 3. Comparison of land surface temperature among the major land-cover types.

neighbor algorithm was used. The VNIR and SWIR bands in ASTER images with a pixel size of 15 m were used for extracting biophysical descriptors, and the TIR bands with a pixel size of 15 m were used for computing LST and extracting thermal features.

### 3. Method

#### 3.1. Computation of land surface temperatures

Various algorithms have been developed for converting ASTER TIR measurements to LSTs as reported by the [ASTER Temperature/Emissivity Working Group \(1999\)](#) and [Gillespie et al. \(1998\)](#). However, a universally accepted method is not available at this time for computing LSTs from multiple bands of TIR data such as those found in ASTER data. In this study, we selected ASTER band 13 (10.25–10.95  $\mu\text{m}$ ) to compute LSTs, because the spectral width of this band is close to the peak radiation of the black-body spectrum given off by the urban surface of the study area. Two steps were taken to compute LSTs: (1) converting spectral radiance to at-sensor brightness temperature (i.e., black-body temperature); and (2) correcting for spectral emissivity. We adopted the most straightforward approximation to replace the sensor response function with a delta function at the sensor's central wavelength to invert LSTs with the assumption of uniform emissivity ([Dash et al., 2002](#); [Li et al., 2004](#); [Schmugge et al., 2002](#)). The conversion formula is:

$$T_c = \frac{C_2}{\lambda_c \ln \left( \frac{C_1}{\lambda_c^5 \pi L_\lambda} + 1 \right)}, \quad (1)$$

where  $T_c$  is brightness temperature in Kelvin (K) from a central wavelength,  $L_\lambda$  is spectral radiance in  $\text{W m}^{-3} \text{sr}^{-1} \mu\text{m}^{-1}$ ,  $\lambda_c$  is the sensor's central wavelength,  $C_1$  is first radiation constant ( $3.74151 \times 10^{-16} \text{ W} \cdot \text{m}^{-2} \cdot \text{sr}^{-1} \cdot \mu\text{m}^{-1}$ ), and  $C_2$  is the second radiation constant ( $0.0143879 \text{ m} \cdot \text{K}$ ).

The temperature values obtained above are referenced to a black body. Therefore, corrections for spectral emissivity ( $\epsilon$ )

became necessary according to the nature of land cover. Each of the land-cover categories was assigned an emissivity value according to the emissivity classification scheme by [Snyder et al. \(1998\)](#). The emissivity-corrected LSTs were computed as follows ([Artis & Carnahan, 1982](#)):

$$\text{LST} = \frac{T_c}{1 + (\lambda \cdot T_c / \rho) \ln \epsilon}, \quad (2)$$

where  $\lambda$ =wavelength of emitted radiance (for which the peak response and the average of the limiting wavelengths [ $\lambda = 10.6 \mu\text{m}$ ] ([Markham & Barker, 1985](#)) was used),  $\rho = h \cdot c / \sigma$  ( $1.438 \times 10^{-2} \text{ m} \cdot \text{K}$ ),  $\sigma$ =Boltzmann constant ( $1.38 \times 10^{-23} \text{ J K}^{-1}$ ),  $h$ =Planck's constant ( $6.626 \times 10^{-34} \text{ J} \cdot \text{s}$ ), and  $c$ =velocity of light ( $2.998 \times 10^8 \text{ m s}^{-1}$ ).

[Fig. 2](#) illustrates the LST images derived from two dates of ASTER TIR images. LST by land-cover type was computed and shown in [Fig. 3](#). A temperature gradient was apparent, with LST

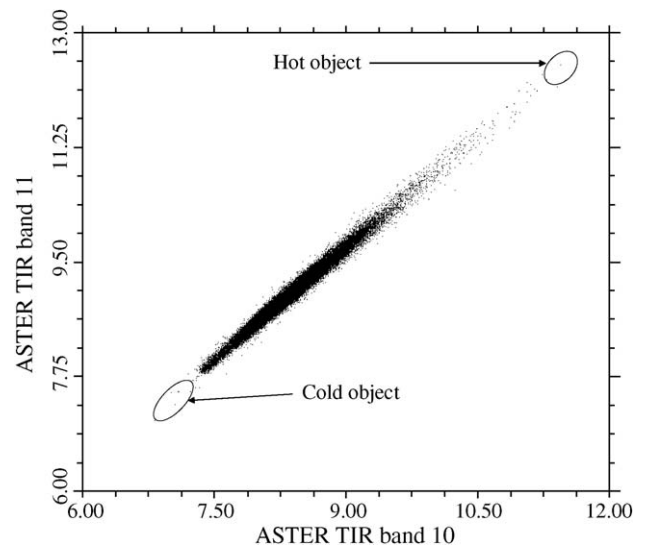


Fig. 4. Scatterplot of ASTER thermal infrared bands 10 and 11 illustrating the selection of hot-object and cold-object endmembers.

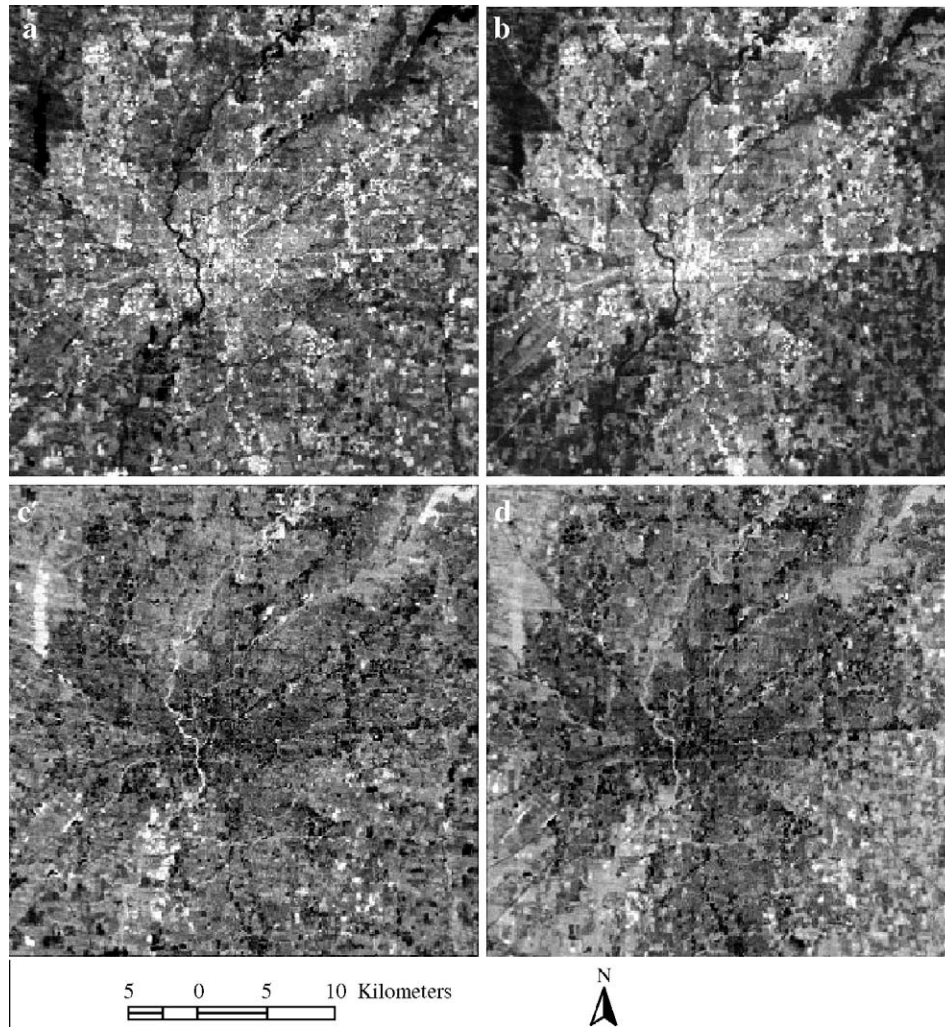


Fig. 5. Hot-object (a and b) and cold-object (c and d) fraction images developed from thermal infrared images of the 2000 and 2001 ASTER data.

decreasing from highest in commercial areas, to medium in high- and low-density residential areas, to lowest in areas with forest and water. Seasonal differences of the LST patterns can be seen in the two LST images, which were taken at different times of the year.

3.2. Introduction to linear spectral mixture analysis

The LSMA approach is based on the assumption that the spectrum measured by a sensor is a linear combination of the

spectra of all components (endmembers) within the pixel, and the spectral proportions of the endmembers reflect proportions of the area covered by distinct features on the ground (Adams et al., 1995). In the LSMA approach, selecting high-quality endmembers is a key for successfully developing high-quality fraction images. In previous research, many methods were developed for endmember selection (Bateson & Curtiss, 1996; Garcia-Haro et al., 1999; Lu et al., 2003; Maselli, 2001; Quarmby et al., 1992; Settle & Drake, 1993; Smith et al., 1990; Theseira et al., 2003; Tompkins et al., 1997; Van der Meer,

Table 1

Correlation coefficients between ASTER bands and principal component analysis results of nine visible, near-infrared, and shortwave-infrared bands of the 2000 and 2001 ASTER data

Bands	VIS1-2	NIR3	SWIR4	SWIR5-9
VIS1-2	0.97 (0.97)	0.04 to 0.13 (−0.16 to −0.21)	0.53 to 0.59 (0.55 to 0.58)	0.71 to 0.80 (0.72 to 0.76)
NIR3			0.40 (0.2)	0.04 to 0.12 (−0.077 to −0.12)
SWIR4				0.81 to 0.89 (0.83 to 0.90)
SWIR5-9				0.97 to 0.99 (0.97 to 0.99)
% of variance	The first four principal components account for 59.70% (66.37%), 38.79% (32.29%), 1.23% (0.87%), and 0.36% (0.45%).			

Values in brackets are for the 2001 ASTER image, and values without brackets are for the 2000 ASTER image. VIS, NIR, and SWIR mean visible band, near-infrared band, and shortwave-infrared band, respectively, in ASTER data.

1999). Image-based endmembers are preferred, because they can be easily obtained from the image feature space and no calibration is needed between selected endmembers and the spectra measured. Image endmembers are frequently derived from the extremes of the image feature space, which are assumed to represent the purest pixels in the images (Mustard & Sunshine, 1999). Another important step in the LSMA approach is the selection of a mathematical solution to unmix the spectral image into fractions. Although different solutions may be used to solve a linear mixture model, the least-squares solution is the most frequently used one due to its simplicity and ease of implementation (Smith et al., 1990; Shimabukuro & Smith, 1991). In this paper, the image-based endmember selection approach was applied to identify two endmembers (i.e., hot object and cold object) from the ASTER TIR bands and to identify five endmembers (i.e., vegetation, soil, low albedo, and two high albedos) from the ASTER VNIR and SWIR bands.

### 3.3. Extraction of thermal features with LSMA

Before LSMA was used to unmix ASTER TIR data, principal component analysis (PCA) was used to convert the five TIR bands into a new data set in order to identify the number of endmembers. The PCA result indicates that the first component accounted for the majority of the variance in the image because of the high correlation between these TIR bands. The first two components accounted for 99.27% and 0.47% of the total variance respectively in the 2000 ASTER image, and 99.40% and 0.42% in the 2001 ASTER image. The correlation coefficients between the TIR bands ranged from 0.983 to 0.997 in 2000 ASTER TIR data and from 0.984 to 0.998 in 2001 ASTER TIR data. Thus, the hot- and cold-object endmembers were selected based on the scatterplots between the TIR images (Fig. 4). The hot-object endmember represented objects with high thermal radiance such as impervious surface, and the cold-object endmember represented objects with low thermal radiance such as vegetation and water. A constrained least-squares solution was then applied to unmix the five TIR bands into hot-object and cold-object fraction images (Fig. 5). The hot-object fraction image displayed high values in commercial areas, medium values in residential areas and bare soils, and low values in forest and water areas. Conversely, the cold-object fraction image showed high values in vegetation and water areas, medium values in agricultural areas, and low values in commercial areas.

### 3.4. Derivation of urban biophysical descriptors with LSMA

Much previous research has indicated that urban biophysical descriptors, such as impervious surface, vegetation abundance, and soil, can be developed from multispectral images using LSMA approach (Lu & Weng, 2004; Small, 2002; Wu & Murray, 2003). The LSMA approach requires that the number of endmembers used cannot be higher than the image bands. In theory, nine endmembers may be developed with the nine VNIR and SWIR bands in the ASTER image. However, high correlation between certain bands (especially

between the six SWIR bands) (Table 1) limited the usage of a large number of endmembers. The NIR band (i.e., band 3) had very low correlation with any of the other ASTER bands, indicating its independence in information. The correlation coefficients between visible bands and between SWIR bands, especially between SWIR bands 5 and 9, were greater than 0.97. The PCA results indicate that the first four components accounted for 99.98% of the overall variance. This suggests that a maximum of five endmembers may be developed in this study.

In urban environments, mixed pixels are very common. The conventional image-based endmember selection approach based on scatterplots of the image bands may not be effective in identifying a sufficient number of endmembers (Lu & Weng, 2004). In this paper, we employed the sequential maximum angle convex cone (SMACC) spectral tool to identify spectral image endmembers (Gruninger et al., 2004). The extreme points were used to determine a convex cone, which defined the first endmember. A constrained oblique projection was applied to the existing cone to derive the next endmember. The cone was then increased to include a new endmember. This process was repeated until a projection derived an endmember that already existed within the convex cone, or until a specified number of endmembers was satisfied (Gruninger et al., 2004). In this study, 10 endmembers were identified by the SMACC approach. The spectral characteristics of the selected 10 endmembers are illustrated in Fig. 6.

A constrained least-squares solution was applied to unmix the nine VNIR and SWIR bands of ASTER imagery into fraction images. Different combinations of five endmembers, which were selected from the ten endmembers, were tested, and fraction images were visually compared. After analyzing the radiance features of selected endmembers, we ultimately

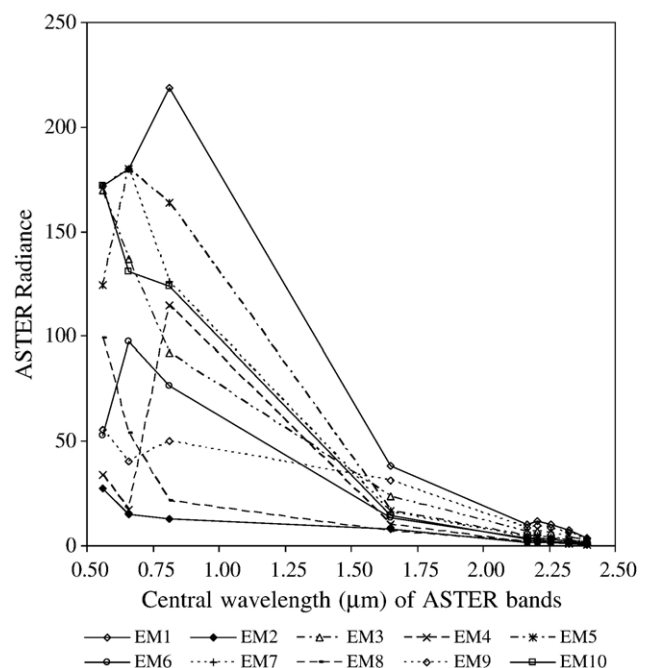


Fig. 6. Radiance curves for selected endmembers.

selected five, namely, vegetation, soil, low albedo, and two high albedos. The high-albedo fraction mainly related to objects with very high reflectance values, such as bright building roofs or construction materials. The low-albedo fraction mainly related to objects with very low reflectance, such as water, canopy shadow, tall building shadows, and dark impervious surface materials.

Previous research indicated that impervious surface can be computed by adding the high- and low-albedo fractions (Wu

& Murray, 2003), but this approach did not consider the impacts of non-impervious surface in the low-albedo fraction image, resulting in overestimation in the areas with non-impervious surfaces, such as water, agricultural lands, and forested areas. Our study of Indianapolis with Landsat ETM+ imagery indicates that the high-albedo fraction mainly represented impervious surface information in the urban area and some dry soils in the agricultural areas. The low-albedo fraction was more complicated. It contained different features,

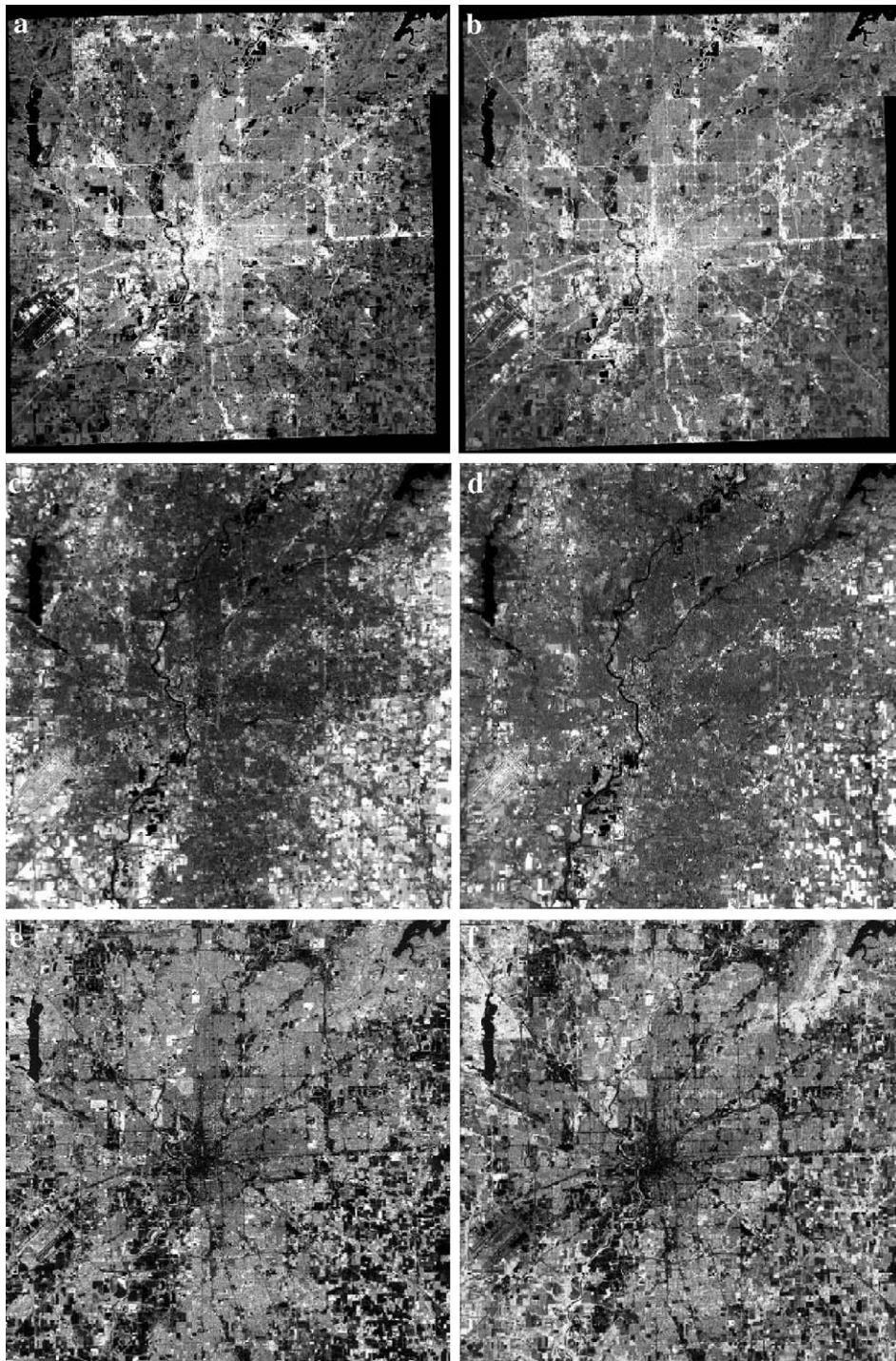


Fig. 7. Impervious surface, soil, and vegetation fraction images developed from 2000 (a, c, and e, respectively) and 2001 (b, d, and f, respectively) ASTER visible, near-infrared, and shortwave-infrared images.

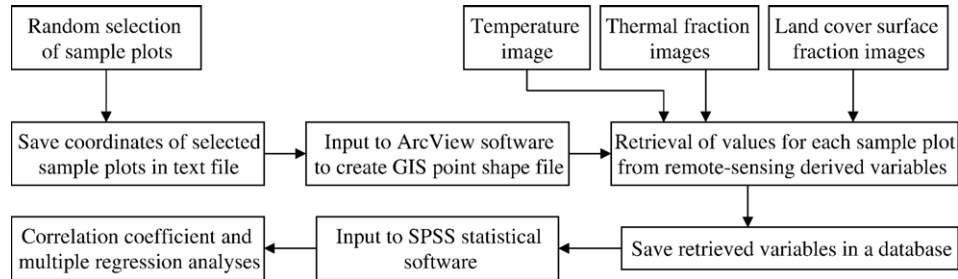


Fig. 8. Framework for retrieval of remote sensing-derived variables for selected samples.

such as water, building shadows in the central business district, vegetation canopy shadows in the forested areas, and dark impervious surface materials (Lu & Weng, 2004). Therefore, it was necessary to remove non-impervious surfaces from high- and low-albedo fraction images before using them to derive impervious surface image. Water bodies, for example, had high values in low-albedo fraction, but no impervious surface existed in the water. Therefore, the pixels of water were first masked out from the low-albedo fraction images with expert rules. An impervious surface image was then produced by adding the adjusted low- and high-albedo fraction images. Fig. 7 illustrates fraction images of impervious surface, soil, and vegetation for the 2000 and 2001 data. In both images, impervious surface fraction values appeared highest in commercial areas and roads, medium in residential areas, and lowest in agricultural lands. In the soil fraction images, the highest values were mainly found in bare soils of agricultural lands. The built-up areas, forests, and water

yielded the lowest values in the soil fraction images. In the vegetation fraction image, the highest values were observed in the areas with grass, crops, and forest. A comparison between the fraction images from the two dates indicates that seasonal differences induced many changes in soil and vegetation proportions, but had little impact on impervious surface coverage.

### 3.5. Relationships between thermal features and biophysical descriptors

Pearson's correlation analysis was conducted to explore the relationships between LST, thermal features (i.e., hot-object and cold-object fractions), and biophysical descriptors (i.e., vegetation abundance, impervious surface, and soil fractions) by land-cover classes at the pixel size ranging from 15, 30, 60, to 90 m. The four land-cover classes examined were (1) commercial-dominated lands (COMM) (i.e., commercial and

Table 2  
Relationships between land surface temperature and remote sensing-derived variables by land-cover classes

Spat Res	Biop Desc	October 3, 2000				June 25, 2001			
		COMM	RESI	FORE	AGRI	COMM	RESI	FORE	AGRI
15 m	Hot	0.726	0.726	0.793	0.603	0.801	0.786	0.896	0.771
	Cold	-0.602	-0.588	-0.642	-0.441	-0.606	-0.561	-0.726	-0.570
	Imp	0.454	0.484	0.008	-0.193	0.534	0.525	0.279	0.014
	Soil	-0.101	-0.059	0.450	0.359	-0.075	-0.032	0.499	0.403
	GV	-0.503	-0.472	-0.228	-0.057	-0.551	-0.518	-0.595	-0.453
30 m	Hot	0.777	0.824	0.819	0.639	0.837	0.847	0.910	0.781
	Cold	-0.681	-0.725	-0.682	-0.474	-0.660	-0.665	-0.723	-0.558
	Imp	0.492	0.502	-0.061	-0.208	0.587	0.533	0.384	0.105
	Soil	-0.098	-0.131	0.508	0.425	-0.204	-0.011	0.542	0.363
	GV	-0.448	-0.622	-0.189	-0.109	-0.552	-0.630	-0.633	-0.454
60 m	Hot	0.802	0.870	0.866	0.655	0.865	0.872	0.932	0.793
	Cold	-0.689	-0.779	-0.729	-0.478	-0.695	-0.694	-0.782	-0.568
	Imp	0.587	0.546	0.081	-0.204	0.670	0.673	0.320	0.116
	Soil	-0.076	-0.151	0.666	0.401	-0.220	-0.026	0.618	0.368
	GV	-0.518	-0.699	-0.459	-0.081	-0.613	-0.734	-0.691	-0.474
90 m	Hot	0.870	0.884	0.877	0.701	0.896	0.889	0.943	0.819
	Cold	-0.786	-0.776	-0.768	-0.531	-0.749	-0.734	-0.809	-0.604
	Imp	0.620	0.560	0.321	-0.248	0.751	0.614	0.447	0.069
	Soil	-0.068	-0.148	0.401	0.455	-0.239	-0.034	0.566	0.426
	GV	-0.535	-0.702	-0.515	-0.115	-0.671	-0.682	-0.710	-0.517

Spat Res=spatial resolution; Biop Desc=biophysical descriptor.

Land-cover classes include: COMM=commercial-dominated lands; RESI=high-density residential-dominated lands; FORE=forest-dominated lands; and AGRI=agriculture-dominated lands.

Hot and Cold represent hot-object and cold-object fraction images, respectively, derived from ASTER TIR data.

Imp, Soil, and GV represent impervious surface, soil, and green vegetation fraction images, respectively, derived from ASTER visible, near-infrared, and shortwave-infrared bands.

some high-density residential areas), (2) high-density residential-dominated lands (RESI), (3) forest-dominated lands (FORE), and (4) agriculture-dominated lands (AGRI). Since the original ASTER data, including ASTER VNIR, SWIR, and TIR bands, were resampled to a pixel size of 15 m by 15 m before the image registration, derived LST and all fraction images also had a pixel size of 15 m. In order to examine the impact of different pixel resolutions on the relationships between LST, thermal features, and biophysical descriptors, the pixel size of the extracted images was resampled to 30 m, 60 m, and 90 m, respectively. The vegetation abundance, impervious surface, and soil fraction images were resampled using a cubic convolution algorithm, taking into consideration that the original spatial resolutions for VNIR and SWIR were 15 m and 30 m, respectively, and coarser spatial resolution data contained information from a large area. The LST and hot- and cold-object fraction images were resampled using a nearest-neighbor algorithm, because these images were restored only in a fine pixel size from a coarse resolution.

Multiple regression analysis was further conducted to assess the relative importance of each biophysical variable for explaining LST patterns. The coefficient of determination ( $R^2$ ) was used to evaluate regression model performance. Beta values were computed to measure the changes of different variables on a standard scale, and to indicate how much change in the dependent variable was produced by a standardized change in one of the explanatory variables when the others were controlled. In order to develop regression models, a total of 500 samples were randomly selected. The value of each sample was retrieved based on each derived variable. Fig. 8 illustrates details of our analytical procedure, including: (1) preparing the LST image from TIR data, hot-object and cold-object fraction images from TIR data, and impervious surface, soil, and vegetation fraction images from the VNIR and SWIR bands; (2) selecting samples, exporting and saving the coordinates of selected samples in a text format; (3) converting the text format

data into a GIS point shape file; (4) retrieving values of all variables for each sample; and (5) saving the retrieved variables in a database and importing to the statistical software for analysis.

#### 4. Results

A comparison of LST, impervious surface, and hot-object fraction images indicates a similar spatial pattern, i.e., highest values in commercial areas, medium values in residential areas, and lowest values in vegetation and water areas. It is well known that impervious surfaces and soils have a heating effect through absorbing and holding solar energy, while vegetation has a cooling effect through offsetting absorptive heating by evapotranspiration. Thus, LST increases as impervious surface increases, but decreases as vegetation increases. Forest, crops, and water have cooling effects and exhibited much lower LST values than impervious surface covers, such as commercial/industrial areas and high-density residential areas, which have heating effects.

Table 2 summarizes the results of correlation analysis between LST and remote sensing-derived variables. Some major findings are summarized as follows:

- (1) LST was positively correlated with hot-object fraction, but negatively correlated with cold-object fraction. These correlations were largely independent of land-cover types and seasons. Meanwhile, LST possessed a stronger correlation with the hot-object fraction than with the cold-object fraction. The correlations between LST and hot- and cold-object fractions became stronger as spatial resolution became coarser.
- (2) LST was positively correlated with impervious surface and negatively correlated with vegetation fraction in the built-up areas (i.e., in COMM and RESI). This finding asserts the role of impervious surfaces in heating and vegetation in cooling the urban surfaces.

Table 3  
Regression analysis results based on land surface temperature and biophysical descriptors

Sample	Date	Regression models	$R^2$	Bcold	Bhot	Bimp	Bgv	Bsol
Total	2000	232.843+61.531Cold+87.164Hot	0.740	1.607	2.308	1.790	0.996	1.337
		273.138+23.306Imp+24.464GV+77.237Sol	0.412					
		228.342+70.813Cold+101.843Hot	0.887					
COMM-RESI	2000	283.469+15.804Imp+8.725GV+45.168Sol	0.487	1.751	2.343	1.098	0.411	0.720
		248.216+48.311Cold+68.671Hot	0.604					
		291.711+10.484Imp+7.381GV+23.052Sol	0.195					
FORE	2001	239.531+60.380Cold+90.559Hot	0.873	1.281	2.014	0.803	0.272	0.413
		293.817+10.184Imp+5.831GV+16.750Sol	0.184					
		239.808+53.460Cold+79.622Hot	0.753					
AGRI	2000	278.047+20.114Imp+15.885GV+59.452Sol	0.248	1.574	2.252	1.112	0.522	0.773
		227.102+72.162Cold+98.206Hot	0.863					
		270.374+23.857Imp+14.072GV+85.863Sol	0.464					
AGRI	2001	239.094+57.912Cold+73.839Hot	0.589	1.641	2.129	1.773	1.606	1.634
		279.810+17.433Imp+22.781GV+59.667Sol	0.298					
		239.997+58.940Cold+90.247Hot	0.902					
		277.119+18.161Imp+17.698GV+56.178Sol	0.301			1.465	1.035	1.231

Bcold, Bhot, Bimp, Bgv, and Bsol are the beta values for cold-object and hot-object fractions derived from the five ASTER thermal infrared bands and impervious surface, vegetation, and soil fractions derived from the nine ASTER visible, near-infrared, and shortwave-infrared bands, respectively.

- (3) Seasonal differences had important impacts on the relationship between LST and biophysical descriptors in forests. As with the October 2000 image, sensors captured mostly non-photosynthetic vegetation (NPV) information. LST was thus positively associated with the NPV fraction in the forested area, which was confused with the soil fraction since no NPV endmember was selected in the LSMA approach. LST appeared more strongly correlated with soil fraction than with vegetation fraction. However, in the June 2001 image, sensors mainly captured information of green leaves. LST was then negatively correlated with the vegetation fraction in the forested areas and appeared more strongly correlated with the vegetation fraction than with the soil fraction. Overall, stronger correlations were found in all land-cover classes between LST and the biophysical descriptors in the June 25, 2001 image than with the October 3, 2000 image.
- (4) In agricultural areas, LST was positively correlated with soil fraction. In the October image, when limited vegetation covered the ground, LST was not significantly correlated with vegetation fraction. However, in the June image, where crops largely covered the ground, LST was negatively correlated with vegetation fraction.

The beta values from the multiple regression analyses based on selected samples show the relative importance of explanatory variables (Table 3). When both hot- and cold-object fractions were considered, the hot-object fraction showed more importance in modulating LST patterns than the cold-object fraction. When other biophysical descriptors (i.e., impervious surface, vegetation, and soil) were considered jointly, impervious surface appeared more significant in influencing LST than vegetation and soil fractions, especially in the built-up areas.

## 5. Discussion and conclusions

This paper demonstrates how fraction images derived from an LSMA approach can be used to examine the relationships between LST and urban biophysical descriptors. Our results show that urban thermal features can be characterized by hot-object and cold-object fractions. LST was found to correlate positively with hot objects, but negatively with cold objects. Hot objects such as impervious surface in urban areas and soils in rural areas posed a stronger impact on LST than cold objects such as vegetation. In the built-up areas, impervious surface was always positively correlated with LST, while vegetation had a negative correlation. In forested and agricultural areas, soil was positively correlated with LST, and vegetation had a negative correlation. These findings suggest that an increased proportion of impervious surface would result in a heating effect in urban areas.

This paper has shown the relative importance of impervious surface, vegetation, and soils in influencing LST. In particular, the importance of accurate extraction of impervious surfaces is necessary for urban studies and environmental assessment. The LSMA approach has proven effective in extracting impervious surfaces (Lu & Weng, 2004; Wu, 2004; Wu & Murray, 2003).

However, impervious surface is a complex category, in which different kinds of materials may mix in the same location and may also occur in different locations, such as in buildings and roads. In addition, the spectral features of some impervious surfaces and soils are similar. Separating these two categories of land cover is difficult, especially in agricultural areas. The limited spectral bands in the multispectral data and associated high correlations between certain bands also restrain the selection of a large number of endmembers, which may allow distinguishing various types of impervious surfaces. A potential solution is to use multiple endmember spectral mixture analysis, a recognized better model than the standard LSMA (Okin et al., 2001; Painter et al., 1998; Rashed et al., 2003; Roberts et al., 1998).

## Acknowledgements

The authors acknowledge the financial support of Indiana Space Grant Consortium to Dr. Qihao Weng, NASA funds through Purdue University (Grant No. NGTS-40114-4), for a project entitled “A Seasonal Analysis of Satellite Detected Urban Heat Island Phenomenon in Indianapolis”, and support from the Center for the Study of Institutions, Population, and Environmental Change, Indiana University, through the National Science Foundation (Grant No. 99-06826). The authors would like to express special thanks to the anonymous reviewers for providing constructive suggestions and comments.

## References

- Abrams, M. (2000). The Advanced Spaceborne Thermal Emission and Reflection Radiometer (ASTER): Data products for the high spatial resolution imager on NASA's Terra platform. *International Journal of Remote Sensing*, 21, 847–859.
- Adams, J. B., Sabol, D. E., Kapos, V., Filho, R. A., Roberts, D. A., Smith, M. O., et al. (1995). Classification of multispectral images based on fractions of endmembers: Application to land-cover change in the Brazilian Amazon. *Remote Sensing of Environment*, 52, 137–154.
- Artis, D. A., & Carnahan, W. H. (1982). Survey of emissivity variability in thermography of urban areas. *Remote Sensing of Environment*, 12, 313–329.
- ASTER Temperature/Emissivity Working Group (1999). Temperature/emissivity separation algorithm theoretical basis document, version 2.4. Pasadena: Jet Propulsion Laboratory, California Institute of Technology ([http://eosps.gsfc.nasa.gov/eos\\_homepage/for\\_scientists/atbd/docs/ASTER/atbd-ast-03.pdf](http://eosps.gsfc.nasa.gov/eos_homepage/for_scientists/atbd/docs/ASTER/atbd-ast-03.pdf); accessed 20 August 2005).
- Bateson, A., & Curtiss, B. (1996). A method for manual endmember selection and spectral unmixing. *Remote Sensing of Environment*, 55, 229–243.
- Carnahan, W. H., & Larson, R. C. (1990). An analysis of an urban heat sink. *Remote Sensing of Environment*, 33, 65–71.
- Collins, E. F., Roberts, D. A., & Borel, C. C. (2001). Spectral mixture analysis of simulated thermal infrared spectrometry data: An initial temperature estimate bounded TESSMA search approach. *IEEE Transactions on Geoscience and Remote Sensing*, 39, 1435–1446.
- Dash, P., Gottsche, F. M., Olesen, F. S., & Fischer, H. (2002). Land surface temperature and emissivity estimation from passive sensor data: Theory and practice—current trends. *International Journal of Remote Sensing*, 23, 2563–2594.
- Dousset, B., & Gourmelon, F. (2003). Satellite multi-sensor data analysis of urban surface temperatures and land cover. *ISPRS Journal of Photogrammetry and Remote Sensing*, 58, 43–54.

- Fujisada, H. (1998). ASTER level-1 data processing algorithm. *IEEE Transactions on Geoscience and Remote Sensing*, 36, 1101–1112.
- Gallo, K. P., McNab, A. L., Karl, T. R., Brown, J. F., Hood, J. J., & Tarpley, J. D. (1993). The use of a vegetation index for assessment of the urban heat island effect. *International Journal of Remote Sensing*, 14, 2223–2230.
- Gallo, K. P., & Owen, T. W. (2002). A sampling strategy for satellite sensor-based assessment of the urban heat-island bias. *International Journal of Remote Sensing*, 23, 1935–1939.
- García-Haro, F. J., Gilabert, M. A., & Melia, J. (1999). Extraction of endmembers from spectral mixtures. *Remote Sensing of Environment*, 68, 237–253.
- Gillespie, A. (1992). Spectral mixture analysis of multispectral thermal infrared images. *Remote Sensing of Environment*, 42, 137–145.
- Gillespie, A., Rokugawa, S., Matsunaga, T., Cothen, J. S., Hook, S., & Kahle, A. B. (1998). A temperature and emissivity separation algorithm for advanced spaceborne thermal emission and reflection radiometer (ASTER) images. *IEEE Transactions on Geoscience and Remote Sensing*, 36, 1113–1126.
- Gruninger, J., Ratkowski, A. J., & Hoke, M. L. (2004). The Sequential Maximum Angle Convex Cone (SMACC) endmember model. *Proceedings SPIE, Algorithms for Multispectral and Hyper-spectral and Ultraspectral Imagery*, vol. 5425, pp. 1–14, August 2004. Orlando, FL.
- Kim, H. H. (1992). Urban heat island. *International Journal of Remote Sensing*, 13, 2319–2336.
- Klysiak, K., & Fortuniak, K. (1999). Temporal and spatial characteristics of the urban heat island of Lodz, Poland. *Atmospheric Environment*, 33, 3885–3895.
- Larson, R. C., & Carnahan, W. H. (1997). The influence of surface characteristics on urban radiant temperatures. *Geocarto International*, 12, 5–16.
- Li, F., Jackson, T. J., Kustas, W. P., Schmugge, T. J., French, A. N., Cosh, M. H., et al. (2004). Deriving land surface temperature from Landsat 5 and 7 during SMEX02/SMACEX. *Remote Sensing of Environment*, 92, 521–534.
- Lo, C. P., Quattrochi, D. A., & Luvall, J. C. (1997). Application of high-resolution thermal infrared remote sensing and GIS to assess the urban heat island effect. *International Journal of Remote Sensing*, 18, 287–304.
- Lu, D., Moran, E., & Batistella, M. (2003). Linear mixture model applied to Amazonian vegetation classification. *Remote Sensing of Environment*, 87, 456–469.
- Lu, D., & Weng, Q. (2004). Spectral mixture analysis of the urban landscapes in Indianapolis with Landsat ETM+ imagery. *Photogrammetric Engineering and Remote Sensing*, 70, 1053–1062.
- Maselli, F. (2001). Definition of spatially variable spectral endmembers by locally calibrated multivariate regression analysis. *Remote Sensing of Environment*, 75, 29–38.
- Markham, B. L., & Barker, J. K. (1985). Spectral characteristics of the LANDSAT Thematic Mapper sensors. *International Journal of Remote Sensing*, 6, 697–716.
- Mustard, J. F., & Sunshine, J. M. (1999). Spectral analysis for earth science: Investigations using remote sensing data. In A. N. Rencz (Ed.), *Remote sensing for the earth sciences: Manual of remote sensing*, vol. 3 (3rd ed.) New York: John Wiley & Sons.
- Okin, G. S., Roberts, D. A., Murray, B., & Okin, W. J. (2001). Practical limits on hyperspectral vegetation discrimination in arid and semiarid environments. *Remote Sensing of Environment*, 77, 212–225.
- Painter, T. H., Roberts, D. A., Green, R. O., & Dozier, J. (1998). The effects of grain size on spectral mixture analysis of snow-covered area from AVIRIS data. *Remote Sensing of Environment*, 65, 320–332.
- Phinn, S., Stanford, M., Scarth, P., Murray, A. T., & Shyy, P. T. (2002). Monitoring the composition of urban environments based on the vegetation–impervious surface–soil (VIS) model by subpixel analysis techniques. *International Journal of Remote Sensing*, 23, 4131–4153.
- Quarmby, N. A., Townshend, J. R. G., Settle, J. J., & White, K. H. (1992). Linear mixture modeling applied to AVHRR data for crop area estimation. *International Journal of Remote Sensing*, 13, 415–425.
- Quattrochi, D. A., & Goel, N. S. (1995). Spatial and temporal scaling of thermal infrared remote sensing data. *Remote Sensing Reviews*, 12, 255–286.
- Quattrochi, D. A., & Luvall, J. C. (1999). Thermal infrared remote sensing for analysis of landscape ecological processes: Methods and applications. *Landscape Ecology*, 14, 577–598.
- Rashed, T., Weeks, J. R., Gadalla, M. S., & Hill, A. G. (2001). Revealing the anatomy of cities through spectral mixture analysis of multispectral satellite imagery: A case study of the Greater Cairo region, Egypt. *Geocarto International*, 16, 5–15.
- Rashed, T., Weeks, J. R., Roberts, D., Rogan, J., & Powell, R. (2003). Measuring the physical composition of urban morphology using multiple endmember spectral mixture models. *Photogrammetric Engineering and Remote Sensing*, 69, 1011–1020.
- Roberts, D. A., Gardner, M., Church, R., Ustin, S., Scheer, G., & Green, R. O. (1998). Mapping chaparral in the Santa Monica mountains using multiple endmember spectral mixture models. *Remote Sensing of Environment*, 65, 267–279.
- Roth, M., Oke, T. R., & Emery, W. J. (1989). Satellite derived urban heat islands from three coastal cities and the utilisation of such data in urban climatology. *International Journal of Remote Sensing*, 10, 1699–1720.
- Schmugge, T., French, A., Ritchie, J. C., Rango, A., & Pelgrum, H. (2002). Temperature and emissivity separation from multispectral thermal infrared observations. *Remote Sensing of Environment*, 79, 189–198.
- Settle, J. J., & Drake, N. A. (1993). Linear mixing and the estimation of ground cover proportions. *International Journal of Remote Sensing*, 14, 1159–1177.
- Shimabukuro, Y. E., & Smith, J. A. (1991). The least-squares mixing models to generate fraction images derived from remote sensing multispectral data. *IEEE Transactions on Geoscience and Remote Sensing*, 29, 16–20.
- Small, C. (2001). Estimation of urban vegetation abundance by spectral mixture analysis. *International Journal of Remote Sensing*, 22, 1305–1334.
- Small, C. (2002). Multitemporal analysis of urban reflectance. *Remote Sensing of Environment*, 81, 427–442.
- Smith, M. O., Ustin, S. L., Adams, J. B., & Gillespie, A. R. (1990). Vegetation in Deserts: I. A regional measure of abundance from multispectral images. *Remote Sensing of Environment*, 31, 1–26.
- Snyder, W. C., Wan, Z., Zhang, Y., & Feng, Y.-Z. (1998). Classification-based emissivity for land surface temperature measurement from space. *International Journal of Remote Sensing*, 19, 2753–2774.
- Streutker, D. R. (2003). Satellite-measured growth of the urban heat island of Houston, Texas. *Remote Sensing of Environment*, 85, 282–289.
- Theseira, M. A., Thomas, G., Taylor, J. C., Gemmell, F., & Varjo, J. (2003). Sensitivity of mixture modeling to endmember selection. *International Journal of Remote Sensing*, 24, 1559–1575.
- Tompkins, S., Mustard, J. F., Pieters, C. M., & Forsyth, D. W. (1997). Optimization of endmembers for spectral mixture analysis. *Remote Sensing of Environment*, 59, 472–489.
- Van der Meer, F. (1999). Iterative spectral unmixing (ISU). *International Journal of Remote Sensing*, 20, 3431–3436.
- Voogt, J. A., & Oke, T. R. (2003). Thermal remote sensing of urban climates. *Remote Sensing of Environment*, 86, 370–384.
- Weng, Q. (2001). A remote sensing-GIS evaluation of urban expansion and its impact on surface temperature in the Zhujiang Delta, China. *International Journal of Remote Sensing*, 22, 1999–2014.
- Weng, Q. (2003). Fractal analysis of satellite-detected urban heat island effect. *Photogrammetric Engineering and Remote Sensing*, 69, 555–566.
- Weng, Q., Lu, D., & Schubring, J. (2004). Estimation of land surface temperature–vegetation abundance relationship for urban heat island studies. *Remote Sensing of Environment*, 89, 467–483.
- Wu, C. (2004). Normalized spectral mixture analysis for monitoring urban composition using ETM+ imagery. *Remote Sensing of Environment*, 93, 480–492.
- Wu, C., & Murray, A. T. (2003). Estimating impervious surface distribution by spectral mixture analysis. *Remote Sensing of Environment*, 84, 493–505.
- Yamaguchi, Y., Kahle, A. B., Tsu, H., Kawakami, T., & Pniel, M. (1998). Overview of Advanced Spaceborne Thermal Emission and Reflection Radiometer (ASTER). *IEEE Transactions on Geoscience and Remote Sensing*, 36, 1062–1071.